Calibration of a Versatile Multi-Energy Soft x-ray Diagnostic for WEST long pulse plasmas

O. Chellai,[1] L. F. Delgado-Aparicio,[1] P. VanMeter,[2,3] T. Barbui,[1] J. Wallace,[1] K. W. Hill,[1] N. Pablant,[1] B. Stratton,[1] C. Disch,[4] B. Luethi,[4] and N. Pilet[4]

[1)]*Princeton Plasma Physics Laboratory, Princeton, NJ 08543, USA*
[2)]*Department of Physics, University of Wisconsin-Madison, Madison, WI 53706, USA*
[3)]*Department of Radiology, Mayo Clinic, Rochester, MN 55905, USA*
[4)]*DECTRIS Ltd., Baden-Daettwil 5405, Switzerland*

(Dated: 12 March 2021)
(The author to whom correspondence may be addressed: ochellai@pppl.gov)

A compact multi-energy soft x-ray diagnostic is being installed on the WEST tokamak which was designed and built to test ITER-like tungsten plasma facing components in a long pulse ($\sim$ 1000 s) scenario. The diagnostic consists of a pinhole camera fielded with the PILATUS3 photon-counting Si-based detector ($\lesssim$ 100k pixels). The detector has a sensitivity in the range 1.6—30 keV and enables energy discrimination, providing a higher energy resolution than conventional systems with metal foils and diodes with adequate space and time resolution ($\lesssim$ 1 cm, 2 ms). The lower-absorption cut-off energy is set independently on each one of the $\sim$ 100k pixels, providing a unique opportunity to measure simultaneously the plasma emissivity in multiple energy ranges and deduce a variety of plasma parameters (e.g. T_e, n_Z and ΔZ_{eff}). The energy dependence of each pixel is calibrated here over the range 3—22 keV. The detector is exposed to a variety of monochromatic sources —fluorescence emission from metallic targets— and, for each pixel, the lower energy threshold is scanned to calibrate the energy dependence. The data is fit to a responsivity curve ("*S-curve*") which determines the mapping between the possible detector settings and the energy response for each pixel. The calibration is performed here for three energy ranges: low ($2.3-6$ keV), medium ($4.5-13.5$ keV) and high ($5.4-21$ keV). We determine the achievable energy resolutions for the low, medium and high energy ranges as 330, 640 and 950 eV respectively. The main limitation for the energy resolution is found to be the finite width of the S-curve.

I. INTRODUCTION

A compact multi-energy soft x-ray (ME-SXR) diagnostic is being installed on the WEST tokamak (CEA Cdarache, France) together with a multi-energy hard x-ray (ME-SHR) diagnostic[1] and a compact x-ray Imaging Crystal Spectrometer (cXICS). The main goal of this diagnostic is to provide time and energy-resolved soft x-ray profiles with applications in impurity transport and MHD activity monitoring as well as electron temperature (T_e) profile measurements and impurity density measurements (n_z). The WEST tokamak[2] was designed to test the ITER-like tungsten plasma facing components[3] in a long pulse ($\sim$ 1000 s) scenario. In tokamaks with high-Z wall-facing components such as tungsten, the accumulation of impurities increases the radiated power which affects the overall power balance and seriously restricts the operational domain. The ME-SXR has a sensitivity in the range 1.6–30 keV, and covers the tungsten lines between 2.3 and 12 keV. It enables energy discrimination with adequate space and time resolution ($\lesssim$ 1 cm, 2 ms), providing a high energy resolution and a unique opportunity to measure simultaneously a variety of plasma parameters. The impurity concentration n_Z will be obtained from the emission line of medium to high-Z impurities in the energy range 2.3—12 keV. In addition to measuring plasma impurity concentrations, the ME-SXR will provide electron temperature (T_e) profiles by modelling the slope of the continuum emission in the energy range 10—21 keV, complementing the installed ECE diagnostic which is challenged in the presence of lower-hybrid current drive due to the downshift of the electron gyro-frequency[4].

In this paper, we discuss the energy calibration of the ME-SXR over three energy ranges : low ($2.3-6$ keV), medium ($4.5-13.5$ keV) and high ($5.4-21$ keV). Although there is a risk for saturation, the low energy range will be exclusively used to study the tungsten transport in WEST using the tungsten line emissions between $2.3-6$ keV. The medium energy range will be used to study the tungsten emission in the range 4.5-12 keV. And finally, the high energy range will also cover the tungsten emission in the range 6-12keV but will also be used to reconstruct electron temperature profiles and possibly study the birth of runaway electrons[5]. A similar calibration performed in the hard x-ray range (up to 100 keV) is presented in[1].

In section II, we briefly describe the ME-SXR diagnostic and its elements. In section III, we detail the energy calibration procedure and describe the experimental setup of the calibration. Finally, the results of the calibration are discussed in section IV.

II. THE ME-SXR DIAGNOSTIC

The ME-SXR diagnostic to be installed on the WEST tokamak consists of a pinhole camera fielded with the PILATUS3 Si detector commercialized by DECTRIS ltd. The ME-SXR will be mounted on an equatorial port in such a way that the field of view is maximized and covers most of the plasma cross-section (see Fig. 1(a)). The detector has a depressurized water-cooled can-shaped casing which is isolated from the torus vacuum using a 300 μm beryllium window. The beryllium window acts as a high-pass energy filter and its thickness was chosen such that the 50% transmission occurs

at ≈ 3.5 keV, filtering out the high-intensity low-energy tungsten lines (from 2 keV and below) which would likely saturate the detector.

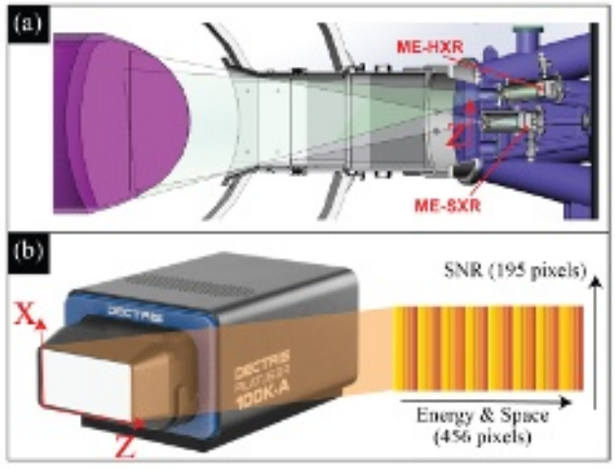

FIG. 1. (a) Schematic view of the ME-SXR in the WEST tokamak. (b) The dectris detector and a possible energy configuration in the WEST tokamak. A detailed explanation of the possible energy configurations and their uses can be found in ref.[6]

.

A. The PILATUS3 Si detector

The PILATUS3 Si detector[7] is an x-ray photon-counting detector based on the reverse-biased diode array technology. The PILATUS3 is made of a single 450 μm silicon detector which absorbs the x-ray photons and convert them into electron/hole clouds by photoelectric effect. The charge cloud is then converted into a voltage pulse by the charge sensitive preamplifiers for each of the 487x195 = 94,965 pixels (often referred to as 100 k) of size 172×172 μm^2 . The voltage pulse is discriminated against a threshold voltage and if the voltage of the pulse is larger than the threshold, it is recorded into a 20-bit counter which is read-out at pre-set intervals. Each one of the pixels has its own charge-sensitive pre-amplifier, a global voltage comparator, a fine 6-bit DAC trimbit setting and counter. By design, the trimbit setting value is an integer between 0 and 63. The pixels are organized into 16 chips containing 60x97 individual pixels. The threshold is set as follows: a global V_{cmp} threshold is set for each chip and the voltage threshold can further be trimmed individually for each pixel using a 6-bit digital to analog converter that we will refer to as the *trimbit* setting $\hat{t}$.

The trimbit setting was initially used to enable homogeneous white plate calibration to account for small inhomogeneities in the electronics. In this paper, we take advantage of a custom calibration of the trimbit setting to set different energy thresholds across the detector. This calibration is explained in detail in the next section.

III. THE ENERGY CALIBRATION

A. Principle of the calibration

The goal of the PILATUS3 calibration is to find the mapping between the trimbit setting $\hat{t}$ and the energy threshold E_{th} for each pixel of the detector, which will be referred here thereafter to as the $\hat{t} - E_{th}$ *curve*. The calibration procedure is similar to the one in[8]. When exposed to a monochromatic source, the response curve of the detector to a scan in the trimbit setting is an error function that is often called an S-curve[6,9]:

$$N(\hat{t}) = \frac{1}{2}\left[\mathrm{erf}(-\frac{\hat{\mathrm{t}} - \mathrm{a}_0}{\mathrm{a}_1\sqrt{2}}) + 1\right](a_2 + a_3(\hat{t} - a_0)) + a_4 + a_5(\hat{t} - a_0), \tag{1}$$

where $N(\hat{t})$ is the number of photon counts. An example of an S-curve measured by a single pixel after being exposed to the 4.51 keV Ti $K\alpha$ emission is shown in Fig. 2. The parameters of interest in this calibration are the inflection point a_0 of the S-curve which corresponds to the trimbit threshold of a pixel for a given incident x-ray energy threshold E_{th} and a_1 which is related to the width of the S-curve and consequently to the achievable energy resolution of the pixel. a_1 is due to electronic noise, charge sharing and the energy spectrum of the incident x-ray. The amplitude a_2 of the error function depends on the flux of the x-ray source and exposure time. The slope a_3 in the linear term models the charge sharing. Finally, a_4 and a_5 describe the linear offset due to the background signal.

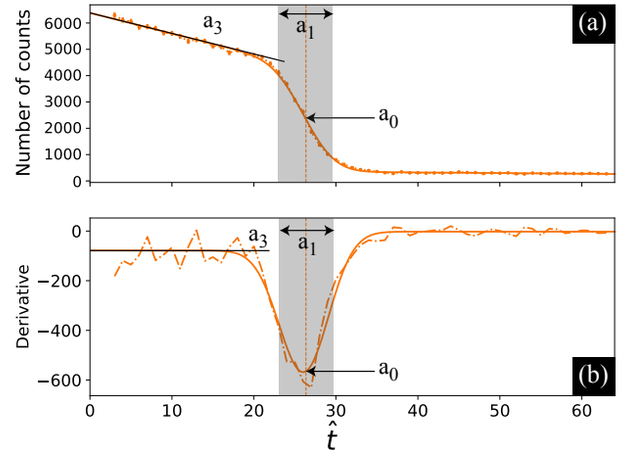

FIG. 2. (a) Example of of the response of a single pixel when exposed to a Ti $K\alpha$ line at 4.51 keV and a scan of the trimbit setting $\hat{t}$. The fit to the function is also shown. The most meaningful parameters of the fits are indicated and the uncertainties in the individual counts are assumed to follow Poisson statistics. (b) Derivatives of the functions shown in (a).

The measurements are performed with several monochromatic x-ray sources (see. section III B) with emissions at dif-

ferent energies. The mapping between the trimbit setting and the energy threshold $\hat{t} = f(E_{th})$ is obtained for each pixel and $f(E_{th})$ is well-approximated by the quadratic function :

$$f(E_{th}) = c_0 E_{th}^2 + c_1 E_{th} + c_2. \quad (2)$$

For each pixel, the experimentally-measured $f(E_{th})$ is fitted to the quadratic function defined in Eq. 2 to ensure the continuity of the mapping. The results of the calibration are discussed in section IV

B. Experimental setup

The measurements for the calibration were performed at DECTRIS Ltd. in Switzerland. X-ray emission from a high-voltage ($50-150$ kV, $25-45$ mA) tungsten tube is emitted towards a rotating wheel on which several metal samples are made availables (see Fig. 3). In each case, either the $L\alpha$ or $K\alpha$ lines from the metal samples (see Tab. I) are re-emitted towards the PILATUS3 detector in such a way that the emission is homogeneous across the detector. The disctinct emission from the $L\alpha$ and the $K\alpha$ emission is achieved by a careful use of voltages in the tungsten tube. 11 metallic targets are used for a total of 15 emission energies ranging between 2.04 keV for zirconium and 24.2 keV for indium. For each emission energy, the trimbit setting $\hat{t}$ is scanned from 0 to 63 and for each $\hat{t}$, the exposure time is set to several minutes, leading to an average exposition time of about 8 hours for each energy calibration range. In the particular cases of Br, Zr and Mo, the $K\beta$ lines (13.30, 17.7 and 19.6 keV, respectively) –although less bright– are also excited.

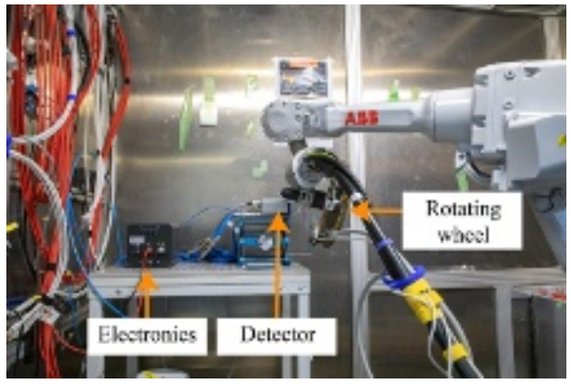

FIG. 3. Experimental setup for the energy calibration. A rotating wheel holds several metal samples. A tungsten tube emits x-ray emission that in turns stimulates the $L\alpha$ and $K\alpha$ line-emission from the metal samples back to the PILATUS3 detector.

IV. RESULTS OF THE CALIBRATION

In the following, the calibration is performed in three energy ranges: low ($2.3-6$ keV), medium ($4.5-13.5$ keV) and high ($5.4-21$ keV) which accessibility is determined by the gain of the pre-amplifier. For each energy range, the trimbit setting scan was performed on each of the $\sim$ 100k pixels. An example of the measured S-curves by a single pixel after being exposed to different metallic line emission is shown in Fig. 4. For better visualization, the curves are normalized so that the response is equal to one when the threshold is half of the threshold corresponding to the incident photon energy. The linear background is also subtracted.

Elements	Zr	Mo	Ag	In	Ti	V	Cr	Fe
Energy lines (keV)	2.04	2.29	2.98	3.29	4.51	4.95	5.42	6.40
	Cu	Ge	Br	Zr	Mo	Ag	In	
	8.05	9.89	11.92	15.77	17.48	22.16	24.2	

TABLE I. Energy of the $L\alpha$ and $K\alpha$ x-ray emission of the metallic targets used in the calibration. The discrimination between the $L\alpha$ and $K\alpha$ lines is performed thanks to a careful use of the x-ray source voltage.

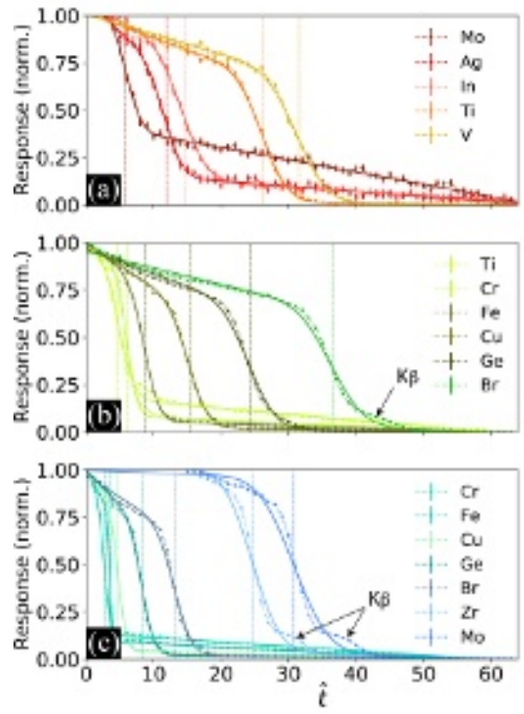

FIG. 4. Fit of the S-curve measured by one single pixel of the detector after being exposed to the x-ray line emission of several elements. (a), (b) and (c) correspond to the low, medium and high energy range, respectively. For visualization purposes, the amplitude is normalized and the linear background subtracted. Uncertainties in the individual counts are assumed to follow Poisson statistics. Dashed lines indicate the inflection point of the curves which corresponds to the a_0 parameter obtained from the fit and the energy from the x-ray source.

The a_0 parameter is identified for each curve in Fig. 4 and the $\hat{t} - E_{th}$ curve is shown in Fig. 5. The error bars and uncertainty of the fits shown in Fig. 5 are representative of all pixels across the detector. In particular, the error bar in the determination of a_0 in the Mo (2.29 keV) measurements is larger

than the other ones because the inflection point of the S-curve occurs close to the limit value of $\hat{t} = 0$. We also found that the energy thresholds corresponding to the Zr $L\alpha$, Ag and In $K\alpha$ lines at respectively 2.04, 22.16 and 24.2 keV are outside the accessible energy threshold range with the gains used for the pre-amplifier, which is the reason why the corresponding results are not displayed here. The bump in the Br, Zr and Mo curves indicated in Fig. 4(b) and (c) is due to the $K\beta$ emission. For those cases, the fluorescence from the L-shell lines fall outside of the measurement range and are not measured. In the future, to improve the accuracy of the determination of the a_0 parameter, a "double S-curve" fit will be used for those elements.

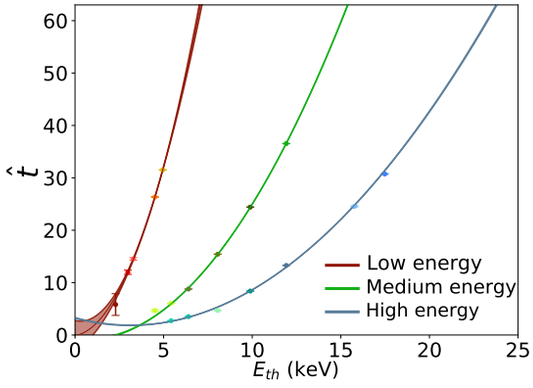

FIG. 5. Trimbit-Energy mapping curve obtained from the a_0 parameters determined in Fig. 4 for the low, medium and high energy ranges. The data points are fitted using a quadratic function (see Eq. 2) and the 1σ uncertainty in the fit is indicated by the shadowed area. The error bars in the data points correspond to the uncertainty in the determination of the a_0 parameter.

A. Accessible energy range and pixel-to-pixel variability

The accessible energy ranges is determined by the trimbit value $\hat{t}$ needed to set the energy threshold E_{th}. As mentioned earlier, the trimbit setting value is an integer between 0 and 63. If the required $\hat{t}$ to set a given E_{th} is outside of this range, the detector cannot be configured properly. The highest achievable energy threshold is therefore given by the energy threshold corresponding to $\hat{t} = 63$. Figure 6 shows the entire set of values taken by the $\hat{t} - E_{th}$ curves by the pixels of the detector for the three calibrations and we notice that this value varies substantially and can differ by several keV from one pixel to the other. Taking into account all the pixels of the detector, we obtain a higher limit for the achievable range of 6, 13.5 and 21 keV for the low, medium and high energy range, respectively. The lowest accessible energy threshold is on the other hand given by the energy of lines that did not provide satisfactory results for the energy calibration since the inflexion points of the S-curve was often found to be at negative $\hat{t}$ values. We find 2.3, 4.5 and 5.4 keV for the low, medium and high energy range, respectively.

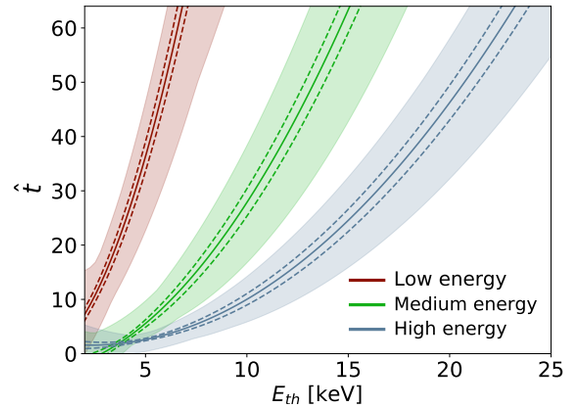

FIG. 6. Trimbit-Energy threshold mapping curves obtained from the a_0 parameters determined in Fig. 4 for the low, medium and high energy range. The shaded area represents the entire set of values taken by all the pixels across the detector. The straight line is the average mapping curve and the dashed lines indicate the standard deviation of the mapping curves.

The quality of the $\hat{t} - E_{th}$ curve fit is investigating by defining χ^2 as $\chi^2 = \sum_s (a_{0,s} - \hat{t}(E_s))/\hat{t}(E_s)$, where E_s is the energy of the x-ray source, $a_{0,s}$ the a_0 parameter obtained by fitting the S-curve corresponding to the energy source s and $\hat{t}(E_s)$ is the trimbit setting corresponding to E_s and given by the $\hat{t} - E_{th}$ curve. The distribution of χ^2 across the detector for each calibration is shown in Fig. 7. The white pixels are either dead pixels or pixels for which either the S-curve or the $\hat{t} - E_{th}$ curve did not provide satisfactory results. The overall quality of the fit if found to be good ($\chi^2 < 1$). In the case of the low energy calibration calibration, some pixels are found to have $\chi^2 > 1$. For this calibration, $\chi^2 > 1$ is caused by a difficulty in determining a_0 in the case of the 2.29 keV L_α emission of Mo. This difficulty in determining a_0 is due to the fact that the $\hat{t} - E_{th}$ curve is pushed to lower $\hat{t}$ values.

B. Energy resolution and limiting factors

There are two main limiting factors for the energy resolution of the detector. The first one is due to the fact that the trimbit setting of the detector is by default an integer. For a desired energy threshold E_{th}, the equivalent trimbit setting $\hat{t}$ can be retrieved from the $\hat{t} - E_{th}$ curve. Often, $\hat{t}$ is a decimal number and must be rounded to the nearest integer value $\hat{T}$ since the trimbit setting applied to the detector is an integer. We define δE as being the standard deviation of $|E_{th}(\hat{t}) - E_{th}(\hat{T})|$, the difference between the requested energy threshold $E_{th}(\hat{t})$ and the effective energy threshold $E_{th}(\hat{T})$. δE as a function of E_{th} is shown in Fig. 8(a) for the three energy ranges. The first observation is that, for each energy calibration, δE is a decreasing function of E_{th}, this is due to the quadratic shape of the energy function. We also see that for all three energy

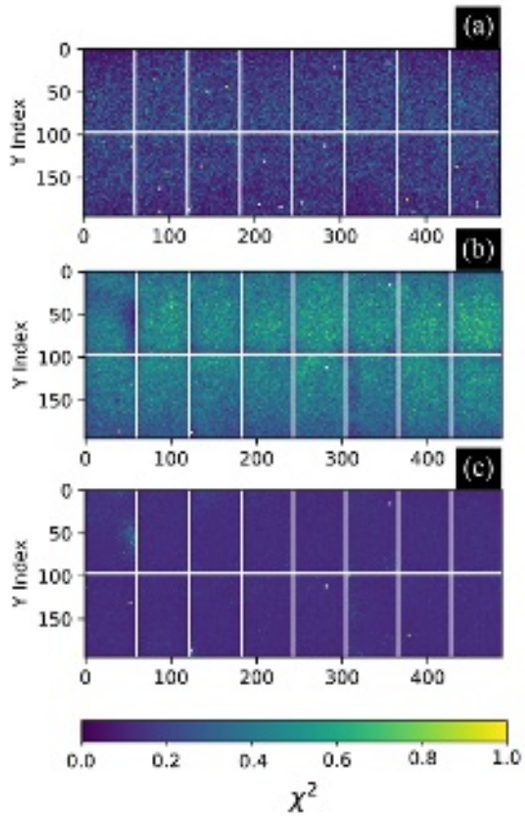

FIG. 7. Distribution of the χ^2 of the $\hat{t} - E_{th}$ curve fit across all the pixels of the detectors. Rows and columns in white represent in-between chips pixels and do not take data. (a), (b) and (c) correspond to the low, medium and high energy range, respectively.

ranges, δE remains small compared to E_{th}. In fact, for the low, medium and high energy range we have: $\delta E < 50$, 100 and 270 eV, respectively, which is $< 0.06\, E_{th}$. We will see in the following that this δE is not the limiting factor for the energy resolution.

The second limit for the energy resolution is related to the width of the S-curve and the a_1 parameter. For an ideal high-pass filter, a_1 would be equal to zero. We have seen however that a_1 has a final width due to electronic noise, charge sharing, the energy spectrum of the incident x-ray and the Fano factor. The impact of the finite value of a_1 on the energy resolution can be estimated by computing $\Delta E = |E_{th}(a_0 + \frac{a_1}{2}) - E_{th}(a_0 - \frac{a_1}{2})|$. The results are shown in Fig. 8(b). Here, we find that the achievable energy resolutions for the low, medium and energy ranges are 330, 640 and 950 eV respectively.

V. CONCLUSION

In summary, we have presented the calibration of the PILATUS3 detector of the novel ME-SXR diagnostic over three energy ranges of interest for impurity transport studies and electron temperature profile measurements : the low ($2.3 - 6$ keV), medium ($4.5 - 13.5$ keV) and high ($5.4 - 21$ keV). The achievable energy resolutions is found to be mainly limited by the width of the response-curve of the detector when exposed to a monochromatic source. This finite width of the S-curve is due to electronic noise, charge sharing and the energy spectrum of the incident x-ray. For the low, medium and high energy ranges, we find an energy resolution of 330, 640 and 950 eV respectively.

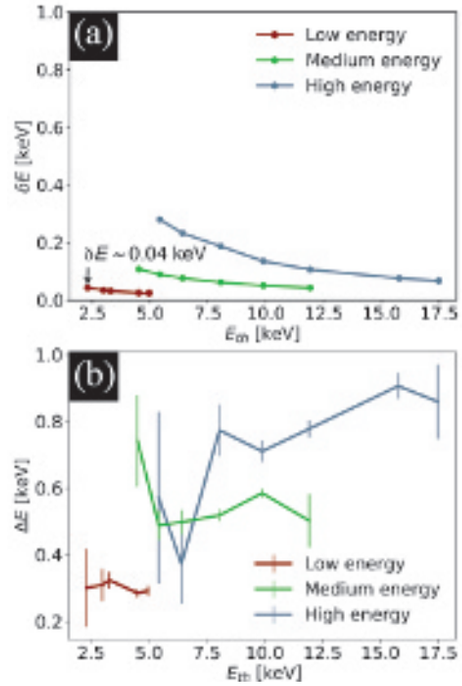

FIG. 8. (a) Standard deviation of the difference between the requested energy threshold and the effective energy threshold due to the rounding of the trimbit setting. (b) Energy resolution of the detector as a function of the energy threshold constrained by the width of the S-curve. The error bars represent the standard deviation of the distribution of the energy resolution for all the pixels across the detector.

VI. ACKNOWLEDGMENTS

This work is supported by the U.S. DOE-OFES under Contract No. DE-AC02-09CH11466.

VII. DATA AVAILABILITY STATEMENT

The data that support the findings of this study are available from the corresponding author upon reasonable request.

[1]T. Barbui, at this conference.
[2]C. Bourdelle *et al.*, Nuclear Fusion **55**, 063017 (2015).

[3]R. Pitts, S. Carpentier, F. Escourbiac, T. Hirai, V. Komarov, A. Kukushkin, S. Lisgo, A. Loarte, M. Merola, R. Mitteau, *et al.*, Journal of Nuclear Materials **415**, S957 (2011).
[4]L. F. Delgado-Aparicio, J. Maddox, N. Pablant, K. Hill, M. Bitter, J. E. Rice, R. Granetz, A. Hubbard, J. Irby, M. Greenwald, E. Marmar, K. Tritz, D. Stutman, B. Stratton, and P. Efthimion, Review of Scientific Instruments **87**, 11E204 (2016).
[5]L. F. Delgado-Aparicio, at this conference.
[6]P. VanMeter, L. F. Delgado-Aparicio, L. M. Reusch, and D. J. D. Hartog, Journal of Instrumentation **14**, C09009 (2019).
[7]"Dectris ltd." `https://www.dectris.com/products/pilatus3/overview/`, accessed: 2020-12-23.
[8]P. VanMeter, L. Delgado-Aparicio, L. Reusch, N. Pablant, J. Maddox, M. Rissi, B. Luethi, T. Donath, C. Schulze-Briese, K. Hill, *et al.*, Review of Scientific Instruments **89**, 10G119 (2018).
[9]P. Kraft, A. Bergamaschi, C. Brönnimann, R. Dinapoli, E. F. Eikenberry, H. Graafsma, B. Henrich, I. Johnson, M. Kobas, A. Mozzanica, C. M. Schlepütz, and B. Schmitt, IEEE Transactions on Nuclear Science **56**, 758 (2009).

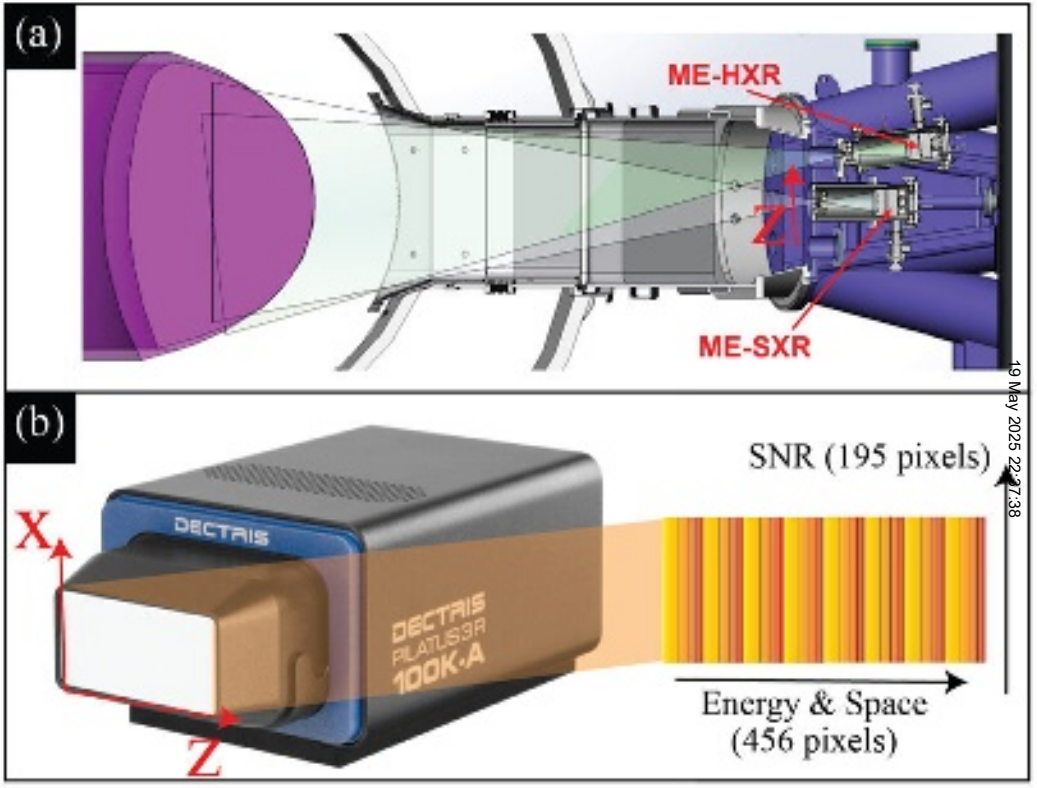

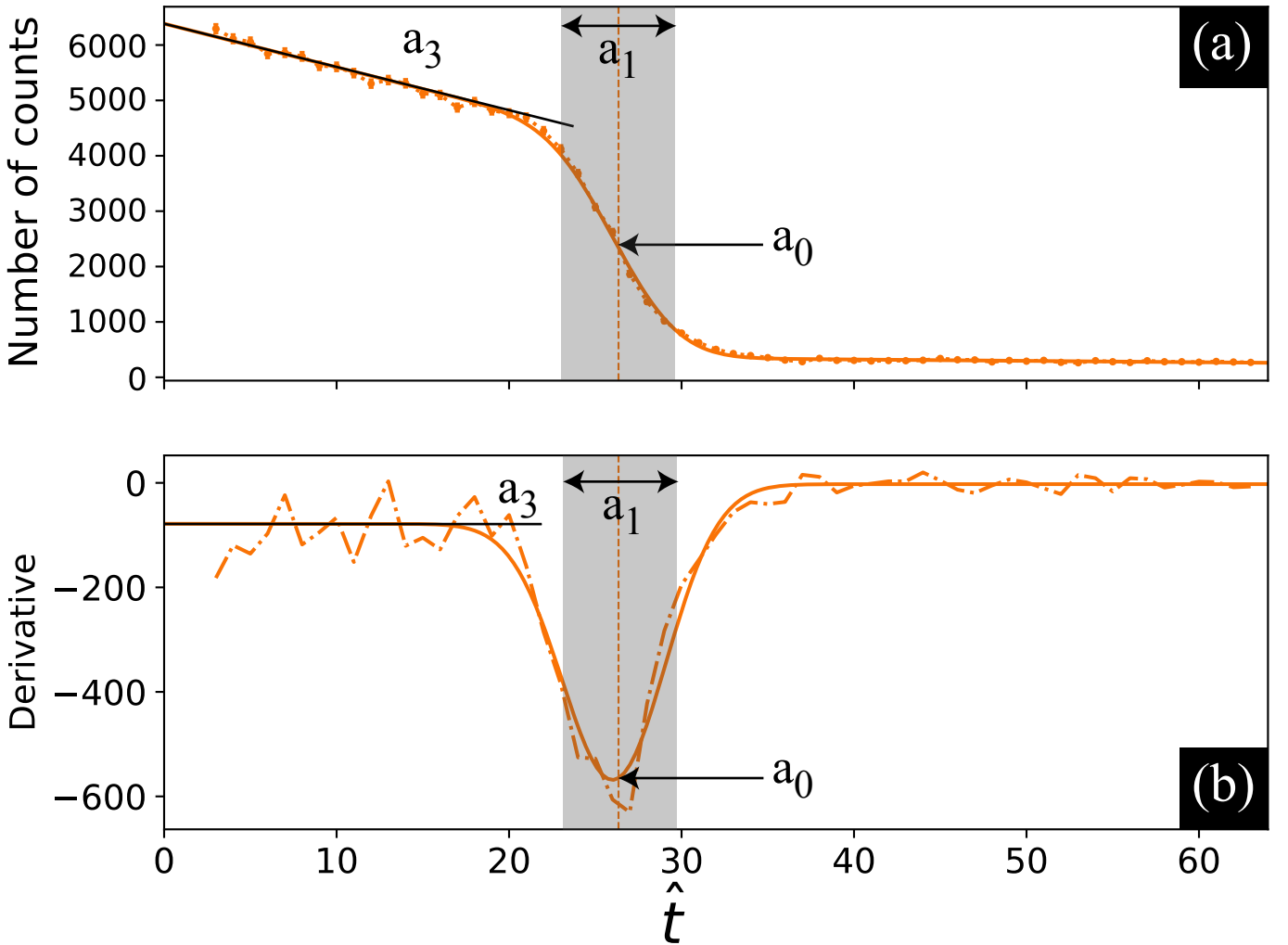

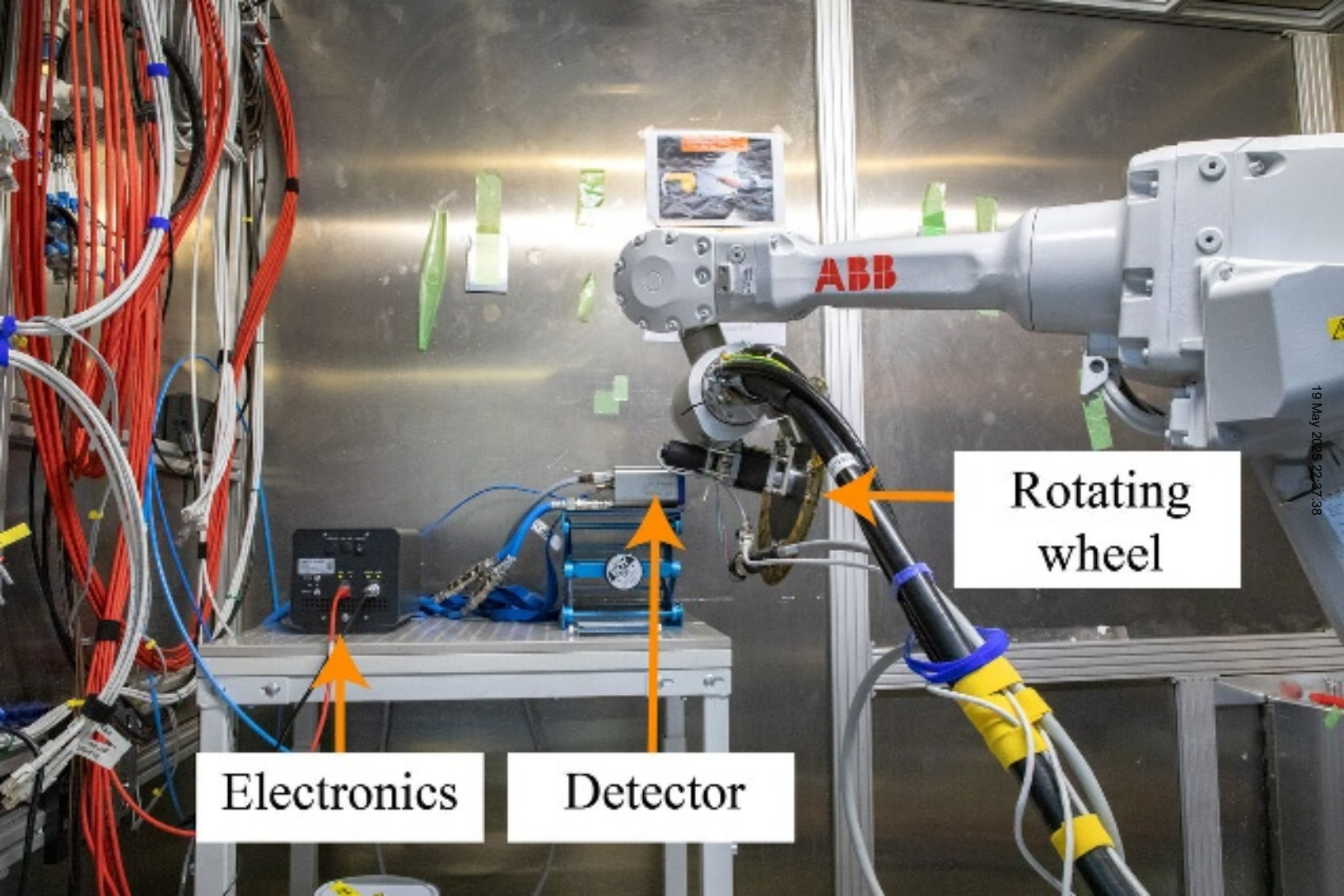
ABB
Rotating wheel
Electronics
Detector